BISTRO: B-fields In STar-forming Regions Observations, an Overview

P. Bastien[1] and the BISTRO Consortium

1. Département de physique et Centre de recherche en astrophysique du Québec, Université de Montréal, C.P. 6128, Succ. Centre-ville, Montréal QC H3C 3J7 Canada

The BISTRO polarimetric survey is currently being carried out with POL-2 and SCUBA-2 on the James-Clerk-Maxwell Telescope (JCMT). It covers the Gould Belt which comprises most of the nearby star-forming regions. More regions have been added to include more massive clouds. The thermal continuum emission at 850 μm from aligned dust grains is linearly polarized and allows the study of magnetic fields in dense molecular clouds which cannot be covered by optical and near-infrared polarimetry. This paper presents a brief overview of results from nine papers. Topics include the morphology of the magnetic field relative to its host filament or cloud, determination of the relative contributions of large-scale and turbulent field components and the strength of the fields in various regions.

1 Introduction

Magnetic fields (**B**-fields) in the interstellar medium (ISM) can be measured since aspherical dust grains are aligned and rotating with their long axis perpendicular to the **B**-field. In the visible/near-infrared the component of the electric radiation field from background stars that is parallel to the grains' long axis is more absorbed, leaving a linear polarization parallel to the plane of sky (PoS) **B**-field component. In the far-IR and submm thermal dust emission is strongest for the orientation parallel to the grains' longest axis. Hence the submm polarization vectors need to be rotated by 90° to trace the PoS **B**-field component.

Rapid progress in submm detector technology in the last 25 years allowed for orders of magnitude improvement in mapping speed of continuum emission from dust grains in molecular clouds. This improvement applies also to polarimeters using those detectors, including POL-2, the JCMT polarimeter. SCUBA-2 is is an innovative 10,000-pixel submm camera with two arrays operating simultaneously at 450 and 850 μm, although only 850 μm data will be discussed here. POL-2 has an achromatic half-wave plate rotating at 2 Hz to modulate the polarization and eliminate most atmospheric effects. It is followed by a wire-grid polarizer. An instrumental polarization due to the membrane in front of the telescope and to many oblique reflexions in the optical train to POL-2 at the Nasmyth focus has been determined and subtracted from all observations. POL-2 was declared commissioned by the East Asian Observatory (EAO) in March 2016.

The Planck satellite (Planck Collaboration et al., 2016) observed magnetic fields across a very wide part of the sky and found that the PoS **B**-field is mostly parallel to filaments in the diffuse ISM or low column density regions and becomes perpendicular to them in dense molecular clouds where the column density $N_{\rm H} > 10^{22}$ cm^{-2}. However, the Planck polarization maps have a resolution of 10 arcmin and do not resolve the filaments and cloud cores where stars form. POL-2 has a resolution of

14 arcsec or 84 times better than Planck and fills a niche between the very large scale surveys and interferometers such as ALMA and SMA. POL-2 resolves easily filaments with a typical width of 0.1 pc and cores in the Gould Belt (see e.g., Fig. 4 below) and further away. The BISTRO consortium with about 140 members was granted 224 h for 16 regions[1] in the Gould Belt. The BISTRO-1 survey started observing in April 2016. Previous intensity maps have been obtained with SCUBA-2 at 850 μm and CO (3 – 2) molecular line maps were also obtained with the 350 Ghz heterodyne array HARP in the brightest parts as part of the JCMT Gould Belt survey and were used for region selection. In July 2017 the BISTRO-2 survey was approved for an additional 16 regions. Here we report results for the first seven BISTRO-1 regions observed and published.

2 The BISTRO Survey

The scientific goals of the BISTRO surveys include:

- Map magnetic fields within cores and filaments, on scales of $\sim 1000 - 5000$ AU, in 32 selected regions
- Determine magnetic field strengths
- Investigate the relative importance of fields and turbulence in star-forming regions
- Model the observed magnetic field geometry
- Study the efficiency of grain alignment
- Study the effects of fields on bipolar outflows

All regions are observed with the same telescope, JCMT, and instruments, POL-2 with the submm array camera SCUBA-2, and are processed with the same software, making for easy and reliable comparison of results between different regions.

BISTRO observations started after commissioning of POL-2. Observations of OMC-1 taken during commissioning were completed to reach the target sensitivity of ≈ 2 mJy beam^{-1} for all BISTRO regions. Each region gets 20 observations with a standard DAISY pattern for a total exposure time of 14 h. OMC-1 was the first BISTRO region and became the BISTRO survey paper's main figure, see Fig. 1 (reproduced from Ward-Thompson et al., 2017). Only vectors with signal to noise $P/\delta P > 3$ are included. Comparison with the previous JCMT polarimeter, SCUPOL, yields very good agreement in bright parts of OMC-1 but less so in fainter regions seen by SCUPOL, with the POL-2 map extending further with its larger field of view and better sensitivity. We find the lower density non-self-gravitating north-eastern filament has a field parallel to its length while the field is perpendicular to the main OMC-1 self-gravitating filament, in agreement with theoretical models.

One can see a clear hourglass shape pattern in Fig. 1. Pattle et al. (2017) carried out a DCF analysis (see next section) of the field strength in OMC-1 and a detailed comparison of the magnetic field energy density, the gravitational potential energy density and the energy density in the the BN/KL outflow, which led to the model illustrated in Fig. 2.

[1]We use 'regions' instead of 'fields' to specify parts of sky observed to avoid confusion with B-fields

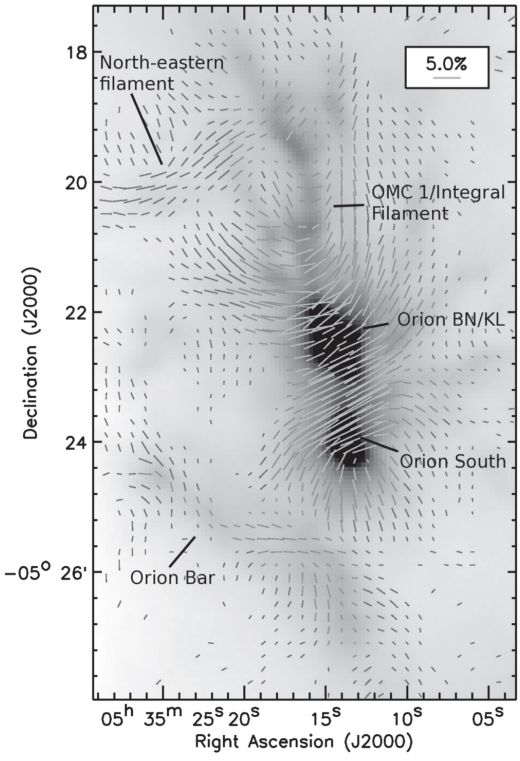

Fig. 1: Magnetic field map of OMC-1 as observed with POL-2 and SCUBA-2 at 850 μm. The polarization vectors have been rotated by 90° to show the orientation of the PoS **B**-field; their length corresponds to the percentage of polarization, with the scale given. The background image is the continuum intensity map obtained with SCUBA-2. This figure is from Ward-Thompson et al. (2017).

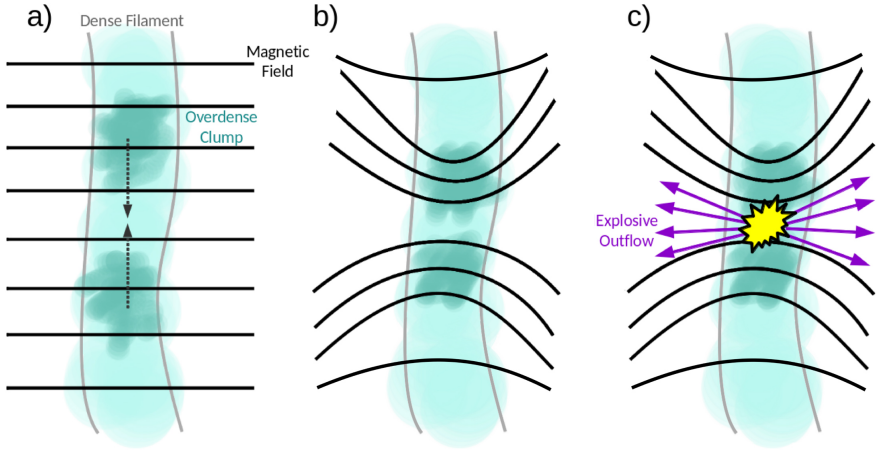

Fig. 2: Cartoon representing our favored model to explain the formation of the hourglass **B**-field morphology of OMC-1. The gravitationally unstable clumps collapse along the filament, dragging the frozen-in magnetic field and controlling the orientation of the BN/KL outflow (Pattle et al., 2017).

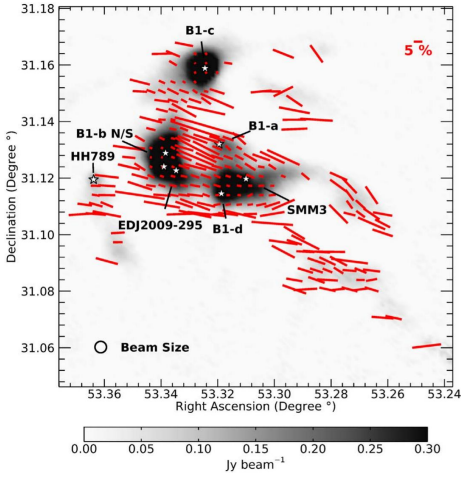

Fig. 3: Perseus B1 polarization map on a 12 arcsec grid superposed on a gray-scale continuum intensity map, both at 850 μm. Individual sources and protostars are identified. The protostellar core B1-c has a bipolar molecular outflow shown with blue and orange arrows in Fig. 4.

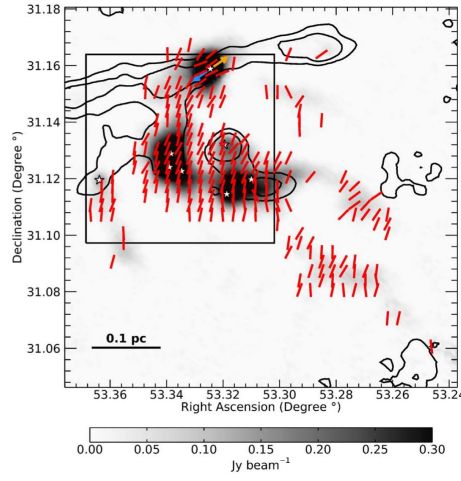

Fig. 4: B1 magnetic field map, with vectors from Fig. 3 rotated by 90° and normalized by length for clarity. The contours show the integrated intensity (10 and 20 K km s^{-1}) of the ^{12}CO $J = 3$–2 molecular line and the box delineates the region used for the DCF analysis.

3 Finding the Strength of the Magnetic Field

The basic hypothesis, turbulent motions that introduce randomness in the morphology of a large-scale magnetic field, was first proposed by Davis (1951). The field is modeled as a uniform magnetic field component with a superposed turbulent component (Chandrasekhar & Fermi, 1953) and its projected PoS component can be written (Crutcher et al., 2004) as

$$B_{\rm pos} = A\sqrt{4\pi\rho}\,\frac{\delta V}{\delta\Phi} \approx \sqrt{4\pi\rho}\,\delta V[\frac{\langle B_t^2\rangle}{\langle B^2\rangle}]^{-1/2}, \qquad (1)$$

where ρ is the density, δV velocity dispersion along the line of sight to the molecular cloud under study and A is a factor of order unity to account for the 3-dimensional nature of the problem. Measuring the dispersion of polarization angles relative to the uniform field, $\delta\Phi$, yields the strength of the PoS **B**-field.

Three ways of doing this leads to different applications of calculating $B_{\rm pos}$ with the Davis-Chandrasekhar-Fermi (Davis, 1951; Chandrasekhar & Fermi, 1953, DCF) method. The dispersion of polarization angles can be obtained: (1) With the standard deviation (SD) of the measured angles, which is the original DCF 1953 method; (2) By using moving boxes (e.g., 3×3 pixels) (Pattle et al., 2017), a method called unsharp masking (UM); (3) With the angular dispersion function (ADF), which is more robust (Hildebrand et al. 2009 and Houde et al. 2009). One computes the difference in position angle between each pair of polarization vectors and takes the mean as a function of separation between them. Note that the dispersion of polarization angles is limited by the dispersion of a completely random sample, $= \pi/\sqrt{12}\,{\rm rad} = 51.96°$

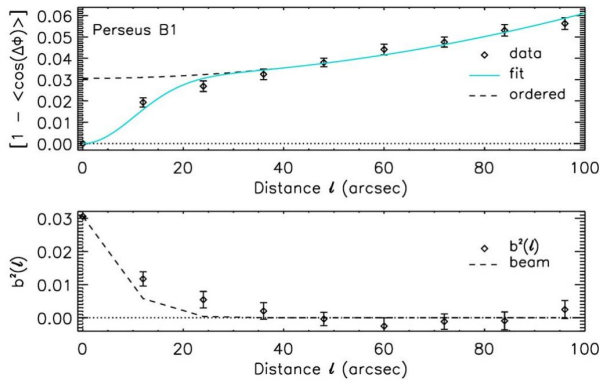

Fig. 5: Top: the angular dispersion function as a function of distance l for B1. Bottom: signal-integrated turbulence autocorrelation function $b^2(l)$ as a function of distance l. Figs. 3, 4 and 5 are from Coudé et al. (2019).

(see Poidevin et al. 2010 and reference therein).

The original DCF method assumes the large scale field is uniform and linear, which does not correspond to reality in most molecular clouds. The standard deviation of polarization angles must be corrected for the uncertainty of the measured values. With the unsharp masking technique, the size of the boxes should take into account the curvature of the field (Koch et al. 2012; Hwang et al., in prep.).

All the BISTRO fields use one or more of the three applications of the DCF method to compute the amplitude of the magnetic field. Here we use Perseus Barnard 1 (B1) as an example of the DCF method. The polarization and magnetic field maps are given in Figs. 3 and 4 respectively. The projected PoS **B**-field is fairly uniform, running mostly North-South, except near the B1-c source where the outflow seems to disturb the **B**-field.

With the ADF application, more information can be obtained in addition to $B_{\rm pos}$, see the second part of Eq. (1), which can be used to compute the ratio of the turbulent to total magnetic energies in the cloud. Other parameters can be derived by fitting the ADF with a Taylor series expansion as a function of the separation between each pair of vectors, l (see details in Hildebrand et al., 2009; Houde et al., 2009; Coudé et al., 2019). The angular dispersion function and the turbulence autocorrelation function are plotted in Fig 5. The results of the DCF analysis for B1 are: PoS **B**-field amplitude $B_{\rm pos} = 120 \pm 60\,\mu$G, ratio of turbulent to total magnetic energy $\langle B_{\rm t}^2\rangle / \langle B^2\rangle = 0.5 \pm 0.3$ and the criticality ratio (Crutcher et al., 2004), $\lambda_{\rm c} = 3.0 \pm 1.5$, which means that B1 is supercritical, its magnetic pressure cannot support the cloud against collapse.

4 Morphology of the B-Field in other BISTRO Regions

Ophiuchus A, B and C in the L1688 molecular cloud in Figs. 6, 7 and 8 show different **B**-field morphologies. In all of them, the general field alignment is parallel to the galactic plane, except in the north-western part of Oph A where it is east-west and in the south-west of Oph B where it is random. Because of their small polarization, only a few starless cores such as Oph C have been observed so far.

The iconic Pillars in M16 were observed in submm polarimetry for the first time by POL-2 (Fig. 9). Many bright B-type stars located north of the pillars ionize the molecular cloud. As described in Fig. 11, the evolution and lifetime of the Pillars in

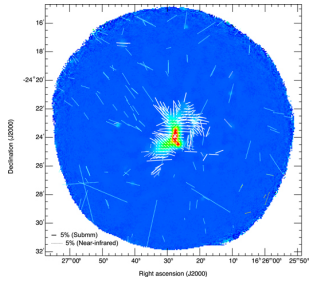

Fig. 6: Ophiuchus A **B**-field map from Kwon et al. (2018). 90°-rotated submm (solid) and (non-rotated) NIR (dotted) vectors are shown. Only vectors with $P/\delta P > 3$ are included.

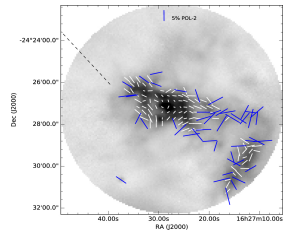

Fig. 7: Ophiuchus B magnetic field map from Soam et al. (2018). White (blue) vectors have $P < 5\%$ ($P > 5\%$). The dashed line is parallel to the galactic plane.

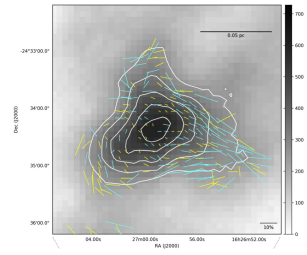

Fig. 8: **B**-field map intensity map at 850 μm zoomed on the core of Ophiuchus C from Liu et al. (2019). Yellow and cyan vectors correspond to data with $P/\delta P > 2$ and $P/\delta P > 3$, respectively.

M16 can be influenced by the strength and orientation of their field.

In our scenario for IC 5146 (Fig. 10) matter falls on the filament following field lines, until eventually it becomes gravitationally unstable. The filament fragments with the more massive clumps at both ends. Those two massive clumps fragment along the curved field lines (Wang et al. 2019; see their Fig. 13).

5 Magnetic Field Strengths in BISTRO Regions

The list of BISTRO papers include the survey paper Ward-Thompson et al. (2017), the seven papers mentioned in Table 1 and a "second generation" paper, Pattle et al. (2019), which studies grain alignment in the three Ophiuchus regions with a Ricean noise model to decrease significantly the bias towards reduced grain alignment in high gas densities compared to what has previously been believed. This allows investigation of magnetic field properties within star-forming clumps and cores.

6 Summary

The BISTRO survey is producing a significant, uniform and coherent database for star formation studies. It maps the detailed configuration of **B**-fields to lower levels than in previous observations. One can quantify the relative importance of uniform vs. turbulent magnetic fields and make a detailed comparison with star formation models. The BISTRO-1 and BISTRO-2 surveys are 100% and 80% complete as of November 2019 and many more papers are in preparation.

Acknowledgements. Detailed acknowledgements for the JCMT operation by the East Asian Observatory, SCUBA-2 and POL-2 construction and all the scientific programs will be found in the individual BISTRO papers. We thank also all the members of the POL-2 construction and commissioning teams who made the BISTRO survey possible.

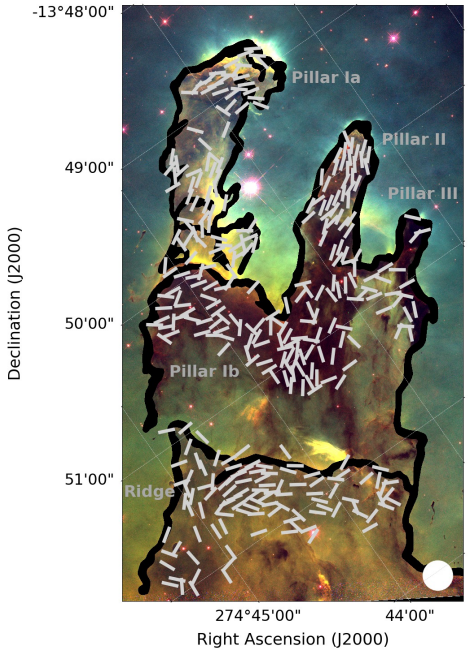

Fig. 9: M16 magnetic field map from Pattle et al. (2018). The map is oversampled for a nicer picture.

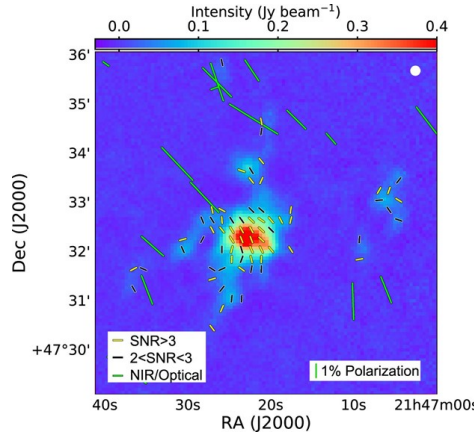

Fig. 10: The *Herschel* satellite showed us that filaments are ubiquitous in molecular clouds. Many of them converge together and form "hubs" such as this one. **B**-field map for the central hub of IC 5146 from Wang et al. (2019).

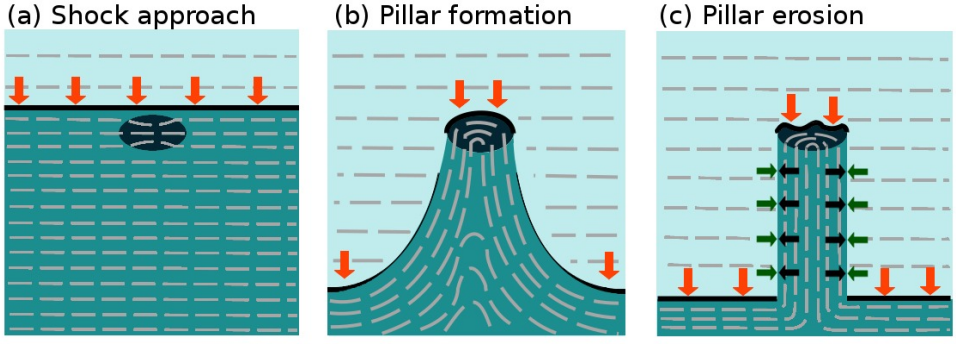

Fig. 11: The proposed evolutionary scenario for M16 (Pattle et al., 2018) is: a) An ionization front moves perpendicularly to the ambient **B**-field; b) The ionization front is slowed down by the over density. The flux-frozen **B**-field bows into the forming pillar; c) The compressed **B**-field supports the Pillar against further gas-pressure and gravity-driven radial collapse, but not against longitudinal erosion by ionizing photons. The pillars longevity results from magnetic support.

Tab. 1: Magnetic field strengths

Source	$B_{\rm pos}$ [μG]	Application[a]	References
OMC-1	6600 ± 4700	UM	Pattle et al. 2017
Oph A	$200 - 5000$	SD	Kwon et al. 2018
Oph B (B2)	630 ± 410	UM	Soam et al. 2018
Oph C	220 ± 110	ADF	Liu et al. 2019
M16 (pillar II)	$170 - 320$	ADF	Pattle et al. 2018
Perseus B1	120 ± 60	ADF	Coudé et al. 2019
IC 5146 (Hub)	400 ± 200	ADF	Wang et al. 2019

[a] The applications used for computing the magnetic field strengths $B_{\rm pos}$ with the DCF method are: UM for Unsharp Masking, SD for the Standard Deviation of polarization angles used in the original DCF method and ADF for the Angular Dispersion Function. They are described in section 3 above.

References

Chandrasekhar, S., Fermi, E., *ApJ* **118**, 116 (1953)

Coudé, S., et al., *ApJ* **877**, 2, 88 (2019)

Crutcher, R. M., Nutter, D. J., Ward-Thompson, D., Kirk, J. M., *ApJ* **600**, 1, 279 (2004)

Davis, L., *Physical Review* **81**, 5, 890 (1951)

Hildebrand, R. H., et al., *ApJ* **696**, 1, 567 (2009)

Houde, M., et al., *ApJ* **706**, 2, 1504 (2009)

Koch, P. M., Tang, Y.-W., Ho, P. T. P., *ApJ* **747**, 1, 79 (2012)

Kwon, J., et al., *ApJ* **859**, 1, 4 (2018)

Liu, J., et al., *ApJ* **877**, 1, 43 (2019)

Pattle, K., et al., *ApJ* **846**, 2, 122 (2017)

Pattle, K., et al., *ApJ* **860**, 1, L6 (2018)

Pattle, K., et al., *ApJ* **880**, 1, 27 (2019)

Planck Collaboration, et al., *A&A* **586**, A135 (2016)

Poidevin, F., Bastien, P., Matthews, B. C., *ApJ* **716**, 2, 893 (2010)

Soam, A., et al., *ApJ* **861**, 1, 65 (2018)

Wang, J.-W., et al., *ApJ* **876**, 1, 42 (2019)

Ward-Thompson, D., et al., *ApJ* **842**, 1, 66 (2017)